J. Fluid Mech. (1993), vol. 255, pp. 11–34

# Unsteady viscous flow over irregular boundaries

By C. POZRIKIDIS

Department of Applied Mechanics and Engineering Science, University of California at San Diego, La Jolla, CA 92093-0411, USA

(Received 26 June 1992 and in revised form 30 March 1993)

Unsteady viscous flow over irregular and fractal walls is discussed, and the flow generated by the longitudinal and transverse vibrations of an infinite periodic two-dimensional wall with cylindrical grooves is considered in detail. The behaviour of the Stokes layer and the functional dependence between the drag force and the frequency are illustrated in a broad band of frequencies for walls with sinusoidal corrugations and a family of walls with triangular asperities leading to fractal shapes. It is shown that, in the case of longitudinal oscillations, the drag force on a fractal wall with self-similar structure exhibits a power-law dependence on the frequency with an exponent that is related to the fractal dimension of the microstructure expressing the gain in surface area with increasing spatial resolution. Numerical evidence suggests that, in the case of transverse oscillations, the dissipative component of the drag force may show a power-law dependence on the frequency, but the exponent is not directly related to the geometry of the microstructure. The significance of these results on the behaviour of the drag force on walls with three-dimensional irregularities is discussed.

## 1. Introduction

Consider a low-amplitude oscillatory viscous flow within a channel with highly irregular walls. At sufficiently high frequencies, the flow is composed of an outer irrotational core and an inner Stokes layer that wraps around the walls. As the frequency is increased, the thickness of the Stokes layer decreases and the interface between the Stokes layer and the potential core penetrates into the finer corrugations. Since the Stokes layer feels an increasingly larger effective boundary surface area, one may argue that the drag force on the wall and rate of viscous dissipation in the fluid tend to obtain increasingly larger values. Furthermore, one may conjecture that if the wall has a self-similar microstructure with an infinite surface area, the drag force and rate of dissipation will tend to diverge at an algebraic rate, but the exponent will not necessarily be related to the fractal dimension of the wall expressing the gain in wall surface area with increasing resolution (Johnson, Koplik & Dashen 1987).

To assess whether the rate of dissipation within channels with self-similar indentations does indeed diverge, Koch (1987) carried out an asymptotic analysis of oscillatory flow within a two-dimensional channel with self-similar rectangular crevices. Assuming that the lengthscales of the crevices are widely separated and then solving for the outer potential flow, he found that the rate of dissipation diverges for a restricted class of geometries, including shapes with finite surface area. Furthermore, assuming that the rate of dissipation is proportional to the effective surface area seen by the Stokes layer, as measured by a yardstick whose lengthscale is equal to the nominal thickness of the Stokes layer, Koch concluded that even when the rate of dissipation diverges, it does not do so in a manner that is related directly to the geometrical features of the wall microstructure.

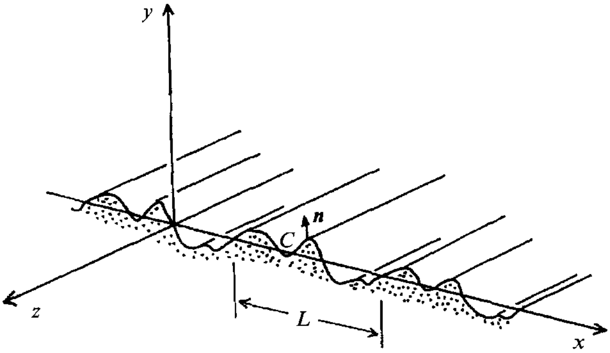

FIGURE 1. Schematic illustration of an irregular wall with cylindrical periodic grooves. The wall executes longitudinal oscillations along the $z$-axis or transverse oscillations along the $x$-axis generating a Stokes boundary layer.

To provide further evidence on the behaviour of viscous oscillatory flow over rough surfaces, in this paper we present a numerical investigation of viscous oscillatory flow over uneven and irregular walls. The main goal is to illustrate the functional dependence between the drag force and the frequency, thereby assessing whether the presence of an infinite cascade of self-similar irregularities alters the usual scaling laws observed for walls with finite surface area. Another objective is to examine the accuracy of scaling arguments based on the concept of the effective wall surface area seen by the Stokes layer.

We consider a model configuration that is composed of a two-dimensional periodic wall with cylindrical grooves vibrating along or across the generators, as illustrated in figure 1. In the absence of hydrodynamic instabilities, longitudinal oscillations along the $z$-axis produce unidirectional flow along the generators, whereas transverse oscillations along the $x$-axis produce a two-dimensional flow in the $(x, y)$-plane. At low frequencies, the nominal Stokes-layer thickness $\delta = (\omega/\nu)^{\frac{1}{2}}$ is considerably larger than the scale of the irregularities, and far from the wall the flow resembles that due to the oscillations of a flat plate; here $\omega$ is the frequency of oscillations and $\nu$ is the kinematic viscosity of the fluid. At large frequencies, $\delta$ is comparable to the characteristic size of the irregularities, and the Stokes layer penetrates into the corrugations with a local intensity that depends upon both the direction of motion and the geometry of the microstructure.

To simplify the analysis and computations, we shall assume that, in the case of transverse oscillations, the amplitude of the motion is sufficiently small compared to the size of the grooves that nonlinear convective forces are small compared to viscous and acceleration forces and the flow is governed by the linear equations of unsteady Stokes flow. This assumption allows us to use efficient numerical methods based on boundary integral formulations and conformal mapping. The significance of linearization for highly irregular and fractal walls and the effects of inertia will be addressed in §§3 and 4.

In §2 we consider the flow generated by the longitudinal oscillations of smooth and fractal walls, discuss the asymptotic behaviour at high frequencies, and present numerical results for sinusoidal walls and a family of walls with triangular asperities leading to fractal shapes. The computations will demonstrate explicitly that the presence of an infinite cascade of self-similar boundary irregularities alters the usual functional relationship between the drag force and the frequency at sufficiently small Stokes-layer thicknesses. We shall show that the usual scaling law must be replaced by an alternative law that involves the fractal dimension of the microstructure expressing the gain in wall length with increasing spatial resolution. In view of the strong restriction on the direction of motion, however, these results will not be claimed to have a general applicability.

In §3 we consider the corresponding problem for transverse oscillations. Several previous authors have considered unsteady flow over corrugated walls with emphasis on describing the onset of steady streaming motion due to inertial effects, and assessing the significance of boundary corrugations on fluid advection and mixing (Lyne 1971; Kaneko & Honji 1979; Sobey 1980; Ralph 1986). We shall consider sinusoidal walls with large-amplitude corrugations and walls with self-similar microstructure. We shall demonstrate that the leading-order contributions to the drag force is due to the added mass of the grooves, which is finite even when the wall has an infinite length, whereas the leading-order dissipative contribution to the drag force is proportional to a drag coefficient, whose value is likely to diverge as the geometry of the wall becomes more refined. This behaviour allows for an algebraic dependence of the drag force on the frequency, but the numerical results suggest that this functional form does not involve the fractal dimension of the wall in a direct manner.

We conclude in §4 by discussing the behaviour of walls with three-dimensional irregularities and commenting on the significance of these results within the general context of transport processes across irregular and fractal boundaries.

## 2. Longitudinal oscillations

We consider the flow generated by an infinite wall with cylindrical grooves oscillating along the $z$-axis with velocity $w = V\exp(\mathrm{i}\omega t)$, as illustrated in figure 1. The Stokes solution for the flow generated by the vibration of a flat plate will serve as a point of reference for assessing the effect of the corrugations (Landau & Lifshitz 1987, p. 83). This solution shows that the magnitude of the drag force per unit area on the plane wall is proportional to $\omega^{\frac{1}{2}}$ or $1/\delta$ where $\delta = (\nu/\omega)^{\frac{1}{2}}$ is the nominal Stokes-layer thickness. The phase shift between the drag force and the wall velocity is a constant independent of $\omega$, equal to $-\frac{3}{4}\pi$.

At high frequencies, the Stokes boundary layer wraps around the corrugations with undiminished intensity; locally, the flow resembles that due to the oscillations of a flat plate. Using the Stokes solution we find that as frequency is increased, the drag force per unit width over one period $L$ tends to the finite asymptotic value

$$D = (\mu V/\delta)\,\mathscr{L}\,\mathrm{e}^{-\frac{3}{4}\pi\mathrm{i}}, \tag{2.1}$$

where $\mathscr{L}$ is the wall length defined as the arc length of the trace of the wall over one period in the $(x, y)$-plane. Equation (2.1) may be regarded as a scaling law between $D$ and $\delta$, stating that at high frequencies, the magnitude of $D$ is proportional to $1/\delta$ or $\omega^{\frac{1}{2}}$, but the phase shift is constant, equal to $-\frac{3}{4}\pi$, independent of $\delta$ or $\omega$.

We consider next a wall that contains an infinite sequence of self-similar asperities over each period, so that its trace in the $(x, y)$-plane is a fractal line and $\mathscr{L}$ is infinite. Clearly, (2.1) breaks down, implying that the magnitude of $D$ may not be proportional to $1/\delta$. An alternative scaling law may be derived by arguing that, as the frequency is increased, progressively finer wall structures are felt by the Stokes layer and thus the magnitude of the drag force is proportional to an effective wall length $\mathscr{L}_{eff}$ that is a function of $\delta$, so that $|D| = \mu V \mathscr{L}_{eff}/\delta$ (Johnson *et al.* 1987; Koch 1987).

One plausible choice for $\mathscr{L}_{eff}$ is the length of the wall as measured by a yardstick whose unit length is equal to $\delta$. This suggests a relation of the form $|D| = \mu V f(L/\delta)$,

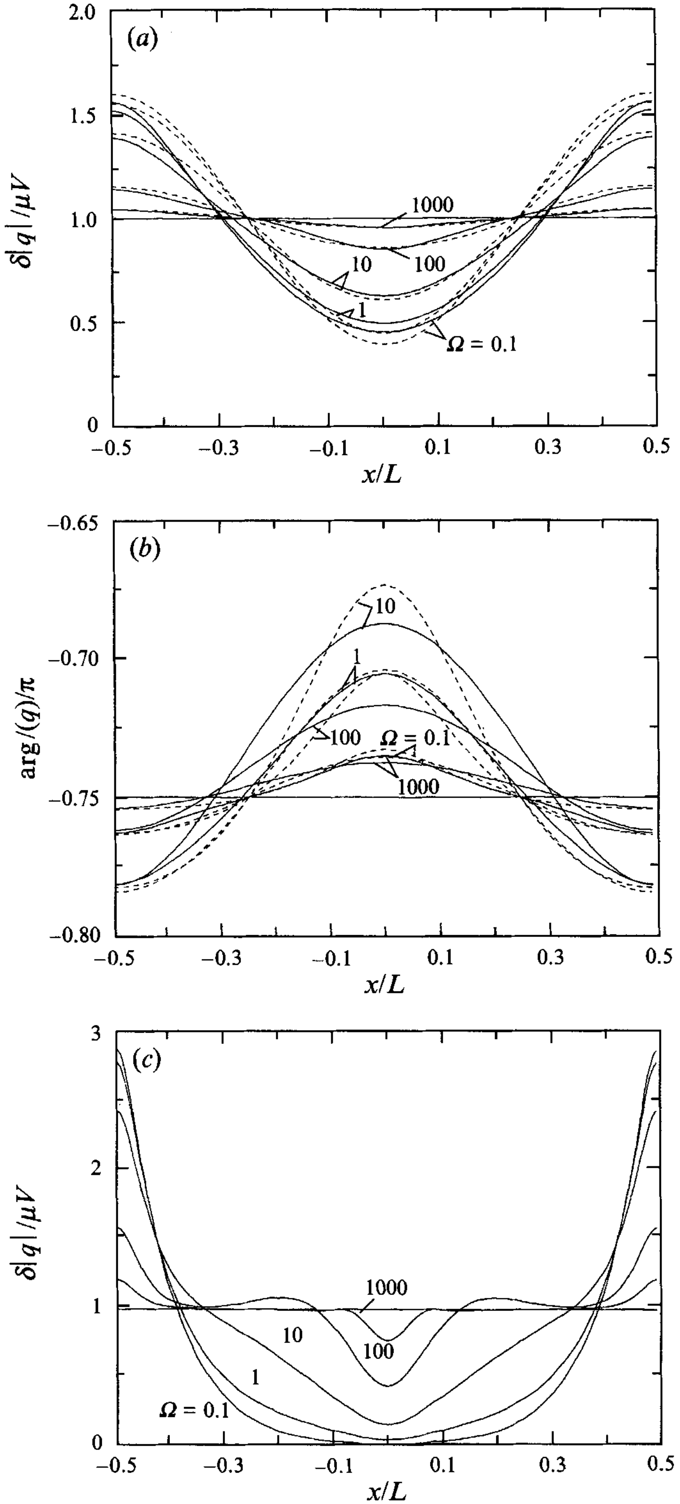

FIGURE 2. For caption see facing page.

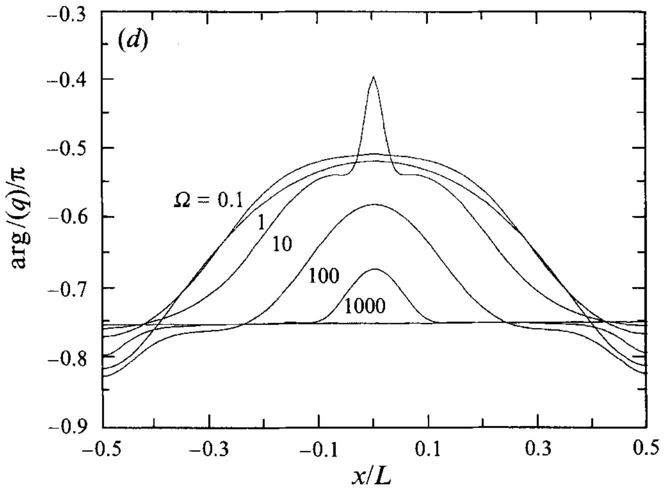

FIGURE 2. The distribution of the reduced magnitude and phase shift of the shear stress $q$ on a sinusoidal wall executing longitudinal oscillations, for several frequencies $\Omega$. Distributions of (*a*) reduced magnitude and (*b*) reduced argument for wall amplitude $a/L = 0.10$; the dashed lines represent predictions of an asymptotic theory for small wall amplitudes. Distributions of (*c*) reduced shear stress magnitude and (*d*) reduced argument for $a/L = 0.50$.

where the function $f(L/\delta)$ depends on the geometry of the wall microstructure. For a wall with an infinite sequence of self-similar irregularities one might expect a power-low relationship of the type $f(L/\delta) = \beta(L/\delta)^{1+d}$, where $\beta$ is a constant and the exponent $d$ expresses the gain in wall length with increasing refinement, yielding

$$|D| \approx \mu V \beta (L/\delta)^{1+d}. \tag{2.2}$$

Note that for a wall with finite length $\beta = \mathscr{L}/L$ is a geometric constant and $d = 0$, so that (2.2) reduces to (2.1). It must be emphasized at this point that the derivation of (2.2) is based upon the premise of effective surface area whose accuracy requires further investigation. Some corroborating evidence will be provided by the results of numerical computations presented in §2.1.

To derive a scaling law for the phase shift of $D$, we replace the fractal wall by a smooth wall whose geometry conforms with the gross shape of the fractal wall as seen by an observer with spatial discrimination of order $\delta$. Further theoretical development, however, necessitates detailed computations and discourages analytical treatment.

To illustrate the practical significance of the modified scaling law (2.2), let us assume that the boundary depicted in figure 1 is set into motion impulsively in the direction of the generators at a constant speed. Taking the Fourier transforms of all flow variables and using the scalings (2.1) or (2.2) we find that the force necessary to move the boundary scales with $t^{-\frac{1}{2}}$ or $t^{\frac{1}{2}(d-1)}$, respectively. Inverting this relation, we find that the velocity during the initial acceleration period of a wall that is set in motion parallel to its generators under the action of an applied constant force increases as $t^{\frac{1}{2}}$ or $t^{\frac{1}{2}(1-d)}$, respectively. These differences suggest that the fractal nature of a wall may be assessed by studying the short-time behaviour during an impulsively started motion.

### 2.1. *Numerical results*

We proceed to illustrate the structure of the Stokes layer and behaviour of the drag force by presenting results of numerical computations for walls with sinusoidal corrugations and families of walls with triangular asperities leading to fractal shapes.

The numerical method is based on a boundary integral formulation outlined in Appendix A. Given the wall geometry, the structure of the flow is considered a function of either the dimensional frequency $\Omega = \omega L^2/\nu$ or the reduced Stokes layer thickness $\delta/L = \Omega^{-\frac{1}{2}}$.

### 2.1.1. *Sinusoidal corrugations*

First, we consider walls with sinusoidal corrugations whose trace in the $(x, y)$-plane is described by the equation $y = -a\cos(2\pi x/L)$. In figure 2(*a*, *b*) we plot the magnitude of the shear stress distribution $q = \mu\nabla w\cdot\boldsymbol{n}$ reduced with respect to the inverse Stokes layer thickness $1/\delta$, and the phase shift $\arg(q)$ reduced by $\pi$, for wall amplitude $a/L = 0.10$. We observe that the distributions of both $\delta|q|/(\mu V)$ and $\arg(q)$ are nearly sinusoidal at all but the highest frequency. Figure 2(*a*) illustrates clearly that the shear stress scales with $\mu V/\delta$ as required by the Stokes flat-plate solution. At large frequencies, the curvature of the wall plays a minor role in determining the local structure of the Stokes layer, and both $\delta|q|/(\mu V)$ and $\arg(q)/\pi$ tend to constant values, equal to 1 and $-\frac{3}{4}$ respectively.

A straightforward asymptotic analysis valid for small values of both $a/L$ and $a/\delta$ shows that to second order in $a/\delta$, the dimensionless wall shear stress distribution is given by

$$\delta q/\mu V = \mathrm{e}^{-\frac{3}{4}\pi\mathrm{i}} + a/\delta(\kappa\,\mathrm{e}^{\frac{1}{4}\pi\mathrm{i}} - \mathrm{i})\cos(2\pi x/L)$$
$$+ (a/\delta)^2\{[\tfrac{1}{4}\mathrm{e}^{-\frac{1}{4}\pi\mathrm{i}} + \tfrac{1}{2}\hat{\delta}(4\pi^2\hat{\delta} - \kappa)\,\mathrm{e}^{\frac{1}{4}\pi\mathrm{i}} - \alpha\rho]\cos(4\pi x/L) + \tfrac{1}{4}\mathrm{e}^{-\frac{1}{4}\pi\mathrm{i}} - \tfrac{1}{2}(2\alpha + \kappa\hat{\delta} + 4\pi^2\hat{\delta}^2)\,\mathrm{e}^{\frac{1}{4}\pi\mathrm{i}}\}, \tag{2.3}$$

where $$\kappa^2 = (2\pi\hat{\delta})^2 + \mathrm{i}, \quad \rho^2 = (4\pi\hat{\delta})^2 + \mathrm{i}, \quad \alpha = \tfrac{1}{4}(2\kappa\,\mathrm{e}^{\frac{1}{4}\pi\mathrm{i}} - \mathrm{i}), \quad \hat{\delta} = \delta/L; \tag{2.4}$$

$\kappa$ and $\rho$ are the square roots of $\kappa^2$ and $\rho^2$ with positive real parts. The first-order predictions of (2.3), represented by the dashed lines in figure 2(*a*, *b*), are in good agreement with the numerical results at all frequencies.

In figure 2(*c*, *d*) we present the shear stress distribution for $a/L = 0.50$ and note some novel features. At low frequencies, the distribution of $\delta|q|/(\mu V)$ has a smooth shape that is characterized by flat minima at the troughs and sharp peaks at the crests, but at higher frequencies, it exhibits noticeable fluctuations. Correspondingly, the distribution of $\arg(q)/\pi$ has a smooth shape at low frequencies and shows local extrema at higher frequencies. These features testify to the complex structure of the Stokes layer. Adopting the deviation of $\arg(q)/\pi$ from the reference value $-\frac{3}{4}$ as a measure of deviation from the local flat-plate solution, we find that, as the frequency is increased, the domain of validity of the flat-plate solution spreads out from the crest to the trough in a progressive fashion.

We turn next to examine the behaviour of the drag force $D$ over one period of the wall illustrated in figure 3(*a*, *b*). We find that at large values of $\delta/L$, the detailed shape of the wall becomes irrelevant and the reduced magnitude of the drag force $\delta|D|/(\mu VL)$ tends to the asymptotic value of unity, whereas the corresponding phase shift tends to $-\frac{3}{4}\pi$. Equation (2.1) states that as $\delta/L$ decreases, $\delta D/(\mu VL)$ must tend to the asymptotic limit $(\mathscr{D}/L)\exp(-\frac{3}{4}\pi\mathrm{i})$; the numerical results shown in figure 3(*a*, *b*) are in agreement with this prediction. It is interesting to note, in particular, that $\delta|D|/(\mu VL)$ passes through a mild maximum before settling to the asymptotic value $\mathscr{L}/L$. The phase shift $\arg(D)$ reaches a maximum at an intermediate value $\delta_{max}/L$ that increases almost linearly with the wall amplitude. This behaviour suggests that $\delta_{max}/L$ scales with the dominant lengthscale of boundary corrugations.

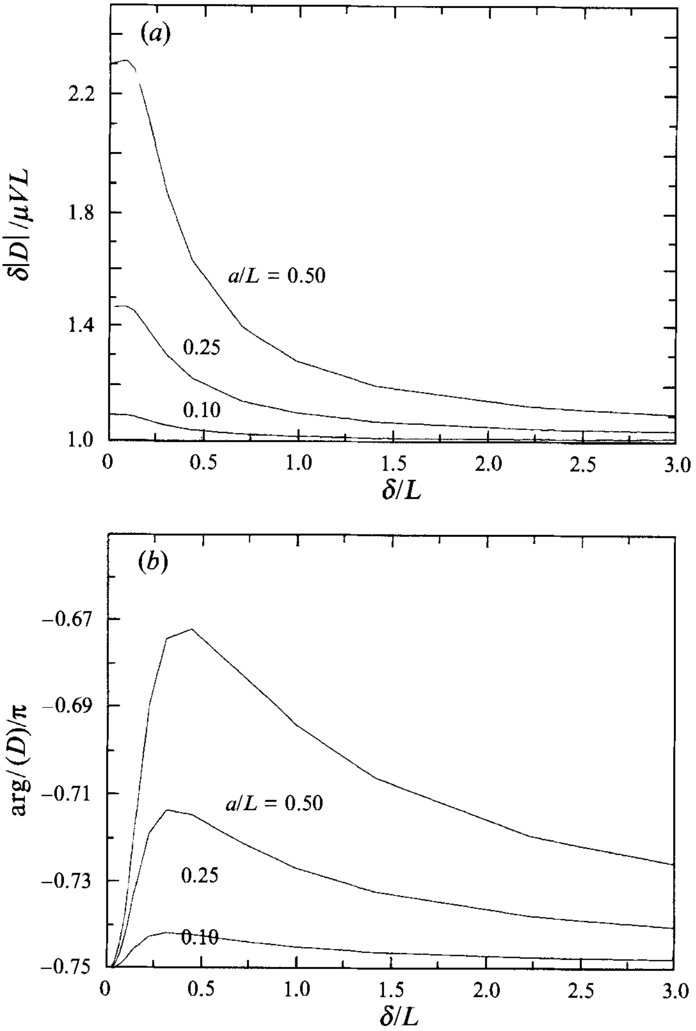

FIGURE 3. (*a*) Reduced magnitude and (*b*) phase shift of the drag force exerted on sinusoidal walls with amplitudes $a/L = 0.10, 0.25, 0.50$, executing longitudinal oscillations.

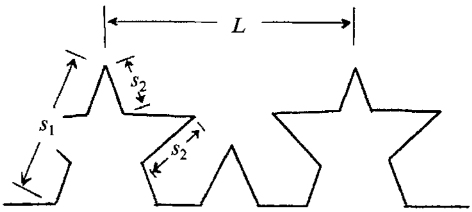

FIGURE 4. Schematic illustration of the trace of a periodic wall with triangular asperities defined by the aspect ratio $\alpha$; $\alpha = 0.50$ yields the von Koch line.

### 2.1.2. *Self-similar asperities and fractal walls*

We proceed next to consider families of walls with self-similar asperities leading to fractal shapes. The geometry of the walls is defined by specifying (*a*) the value of a parameter $\alpha$ that expresses the aspect ratio of the asperities and (*b*) the integer $m$ that

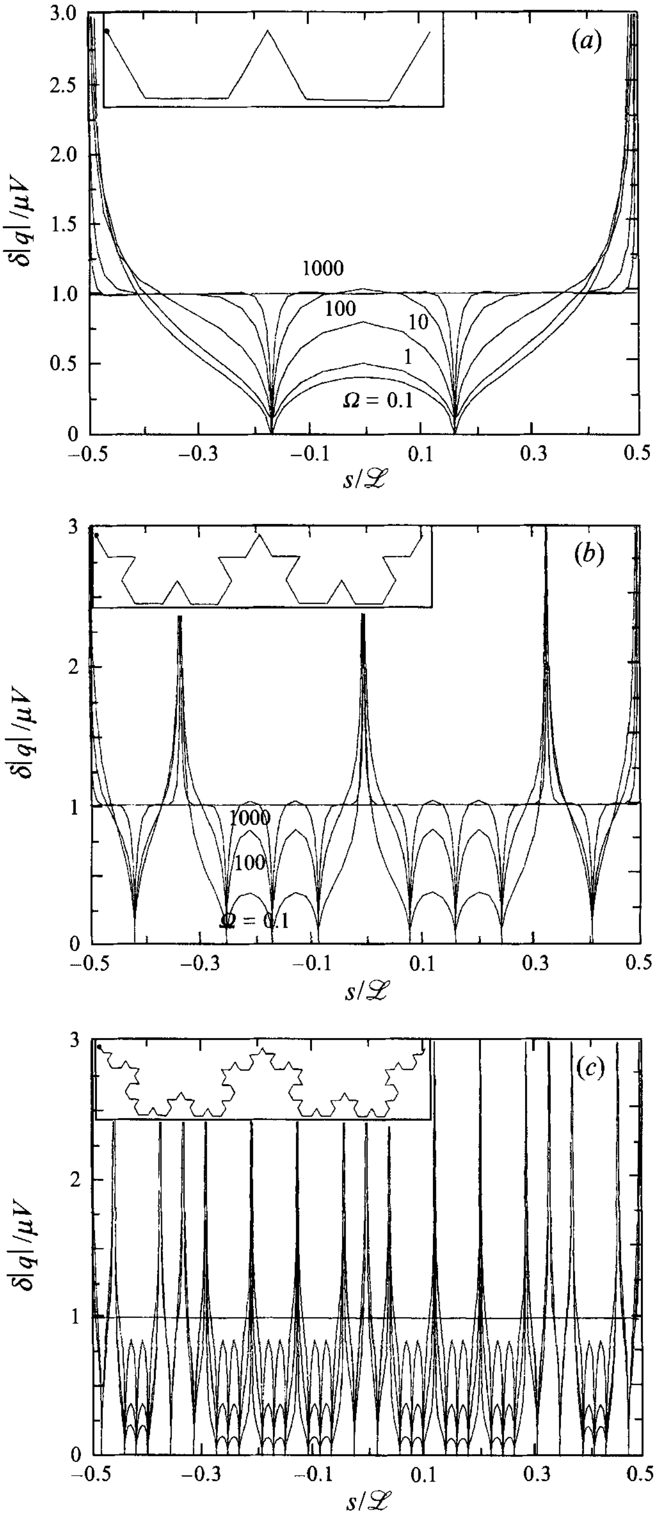

FIGURE 5. For caption see facing page.

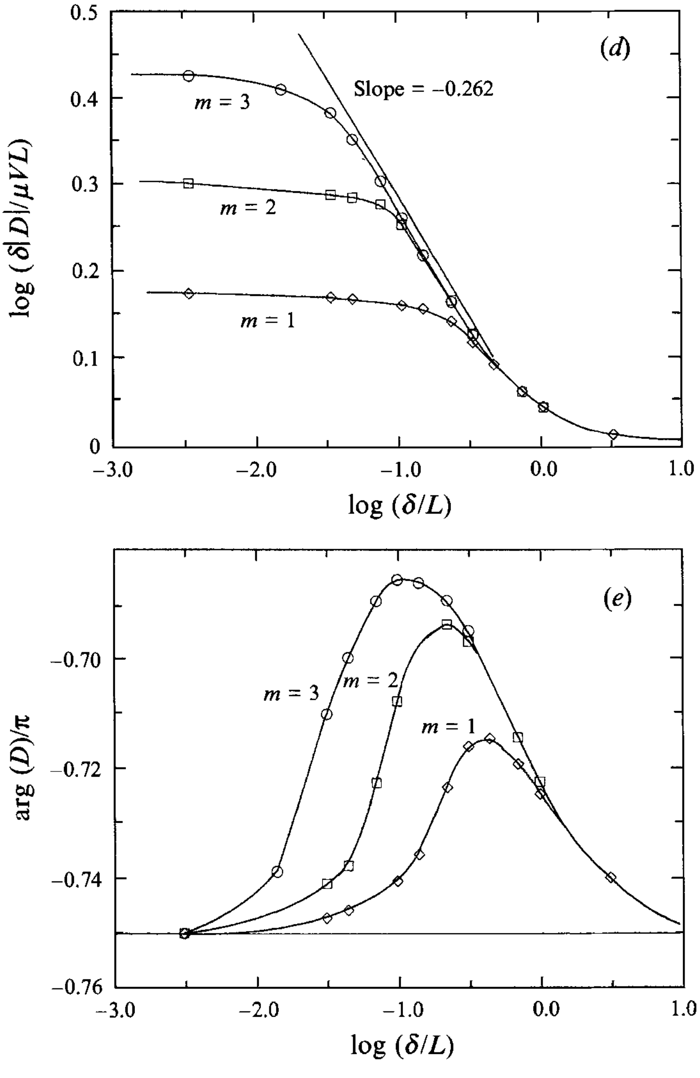

FIGURE 5. The distribution of shear stress over one period on a family of walls with triangular asperities executing longitudinal oscillations for $\alpha = 0.50$ and (*a*) $m = 1$, (*b*) $m = 2$, (*c*) $m = 3$; $s$ is the normalized arclength with $s = -0.50$ corresponding to the leftmost point of the contour shown in the insets. (*d*) The magnitude and (*e*) phase shift of the drag force over one period. The straight line represents the predictions of an effective surface theory expressed by (2.2).

indicates the generation of the wall, as illustrated in figure 4 and in the insets of figures 5(*a–c*), 6 and 9(*a*, *b*). For $m = 1$ the trace of the wall is a straight line with an infinite sequence of triangular asperities, and each time $m$ is increased by one unit, an asperity is added in the middle of each segment. When $\alpha = \frac{1}{3}$ and $m = 1$ the trace of the wall collapses to the $x$-axis, whereas when $\alpha = 1.0$ the asperities become flat plates with infinitesimal thickness. For $\alpha = 0.50$ we obtain the standard von Koch family of self-similar shapes (Feder 1988). The length of the side of the asperities is given by $s_1 = \alpha L$, $s_m = \frac{1}{6}(1+2\alpha)s_{m-1}$ for $m > 1$; the length of the wall over a period is given by $\mathscr{L} = 3L\alpha[\frac{2}{3}(1+2\alpha)]^{m-1}$. Since each time a refinement is effected the length of the wall increases by a factor that is greater than one, as $m$ tends to infinity the length of the wall diverges and the trace of the wall becomes a fractal line.

In figure 5($a$–$c$) we illustrate the distribution of the reduced magnitude of the shear stress for the first three members of the von Koch family corresponding to $\alpha = 0.50$. A local analysis near the corners indicates that the shear stress behaves as $s^{(\pi-\theta)/\theta}$, where $\theta$ is the internal angle of a corner and $s$ is the arclength measured from the vertex; this singularity is accurately manifested in the numerical solution (see Appendix A). At large frequencies, the distribution of $\delta|q|(\mu V)$ tends to the value of unity everywhere except at the corners where it is either infinite or zero. Cursory inspection of figure 5($b$, $c$) shows that the distribution of the shear stress over the individual boundary segments is nearly independent of the location of the segments and is determined primarily by the turning angles at the vertices. This suggests that the local structure of the flow is insensitive to the global geometry of the wall.

In figure 5($d$) we plot the reduced magnitude of the drag force over one period of the wall as a function of $\delta/L$, on a log–log scale. We observe that as $\delta/L$ tends to zero, $\log[\delta|D|/(\mu VL)]$ tends to the asymptotic value $\log(\mathscr{L}/L)$, in agreement with the asymptotic predictions discussed in §2. More importantly, we note that the central portions of the curves for $m = 2, 3$ are nearly straight lines with well-defined, nearly identical slopes. To interpret this behaviour in the context of the scaling law (2.2), we consider the von Koch fractal corresponding to $m = \infty$. We then assume that at a particular value of $\delta/L$, the magnitude of the reduced drag force $\delta|D|/(\mu VL)$ is proportional to an effective wall length $\mathscr{L}_{eff}/L$, and identify $\mathscr{L}_{eff}$ with the length of the $m$th-order von Koch line which is equal to $\frac{3}{2}L(\frac{4}{3})^{m-1}$. The order $m$ is found by setting the length of one segment of the von Koch line equal to $\delta$, i.e. $\delta = \frac{1}{2}L(\frac{1}{3})^{m-1}$. Solving for $m$ and combining with the previous expression we find that, for sufficiently small layer thicknesses, $\log[\delta|D|/(\mu VL)] \approx -d\log(\delta/L)$, where the constant

$$d = -\log(\tfrac{4}{3})/\log(\tfrac{1}{3}) = 0.262$$

is equal to the gain in the length of the von Koch fractal with increasing spatial resolution. The predictions of this scaling law, represented by the straight line in figure 5($d$), are in excellent agreement with the numerical results, thus corroborating the accuracy of the heuristic arguments underlying (2.2).

In figure 5($e$) we plot the reduced phase shift of the drag force $\arg(D)/\pi$, and confirm that it tends to the asymptotic value $-\frac{3}{4}$ both at low and high values of $\delta/L$. Maximum phase shift is attained at a particular value $\delta_{max}/L$ that increases by a nearly constant factor as the wall is refined to the next level. This behaviour suggests that, as in the case of sinusoidal walls, $\delta_{max}/L$ scales with the dominant size of boundary irregularities.

To demonstrate that (2.2) has a more general applicability, in figure 6 we plot the reduced magnitude of the drag force over one period of the wall for asperities with a higher aspect ratio $\alpha = 0.90$ for three generations $m = 1, 2, 3$. The shape for $m = 3$ is illustrated in the inset. Following the above arguments we derive the scaling law $\log[\delta|D|/(\mu VL)] = -d\log(\delta L)$ which is represented by the straight line in figure 6; the constant $d = -\log(5.6/3)/\log(1.4/3) = 0.819$ is equal to the gain in the wall length with increasing spatial resolution. The good agreement between the numerical results and the theoretical predictions provides further evidence for the validity of (2.2) within the class of fractal shapes with triangular asperities considered in this study. In terms of the aspect ratio $\alpha$, the exponent $d$ is given by $d = -\log[\frac{2}{3}(1+2\alpha)]/\log[\frac{1}{6}(1+2\alpha)]$. Note that when $\alpha = 1$, in which case the triangular asperities become flat plates of infinitesimal thickness, $d = 1$.

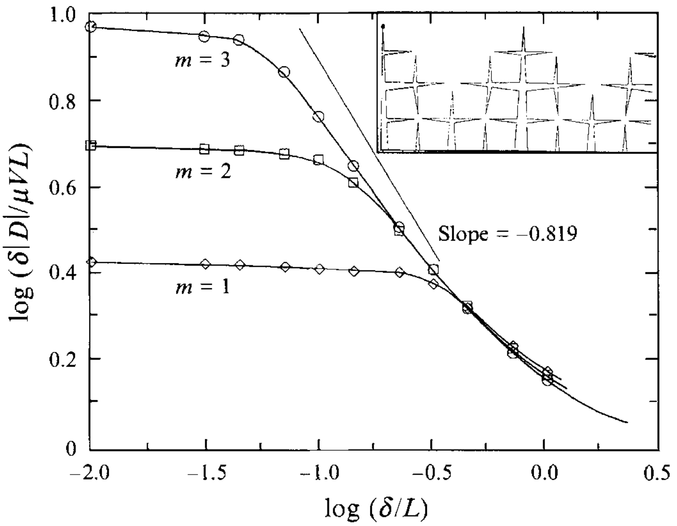

FIGURE 6. The magnitude of the drag force on walls with triangular asperities with $\alpha = 0.90$. The straight line represents the predictions of the effective surface theory expressed by (2.2).

## 3. Transverse oscillations

We proceed to consider the flow generated by transverse oscillations along the $x$-axis with wall velocity $u = V\exp(\mathrm{i}\omega t)$. Assuming that the amplitude of the oscillations is small compared to the lengthscale of the corrugations, we find that the flow is governed by the linearized equation of motion or unsteady Stokes equation (Batchelor 1967, p. 355; Pozrikidis 1992, Chap. 1).

In the case of a wall with self-similar microstructure involving an infinite cascade of lengthscales, linearization will cease to be accurate when the nominal Stokes-layer thickness $\delta$ becomes smaller than a threshold value that is proportional to the amplitude of the wall displacement. At smaller layer thicknesses nonlinear forces will become important and flow instabilities are likely to develop, rendering the motion difficult to analyse and hard to predict. Thus, in this case linearization will be valid only when the limit of large frequencies is taken simultaneously with the limit of correspondingly small amplitudes of oscillation.

At high frequencies, the flow is composed of an outer irrotational regime and the inner Stokes layer. The outer flow exerts on the wall an inertial force due to the virtual mass of the corrugations, whereas the Stokes layer is responsible for a dissipative drag force that is composed of a skin friction and a form drag. Summing these contributions we obtain the asymptotic expansion

$$D = \mu V[\mathscr{m}(L/\delta)^2\,\mathrm{e}^{-\frac{1}{2}\pi\mathrm{i}} + \mathscr{d}(L/\delta)\,\mathrm{e}^{-\frac{3}{4}\pi\mathrm{i}} + \ldots], \tag{3.1}$$

where $\mathscr{m}$ is a dimensionless virtual mass coefficient corresponding to transverse acceleration, and $\mathscr{d}$ is a dimensionless drag coefficient associated with the Stokes layer. Both $\mathscr{m}$ and $\mathscr{d}$ may be computed from knowledge of the boundary distribution of the velocity potential $\phi$ and tangential velocity of the irrotational flow $v$ that is established when the wall is held stationary in an inviscid streaming flow with velocity $V$ parallel to the $x$-axis. We find

$$\mathscr{m} = \frac{1}{VL^2}\int_{Wall}(\phi - Vx)\,n_x\,\mathrm{d}l, \quad \mathscr{d} = \frac{1}{V^2L}\int_{Wall}|v|^2\,\mathrm{d}l \tag{3.2}$$

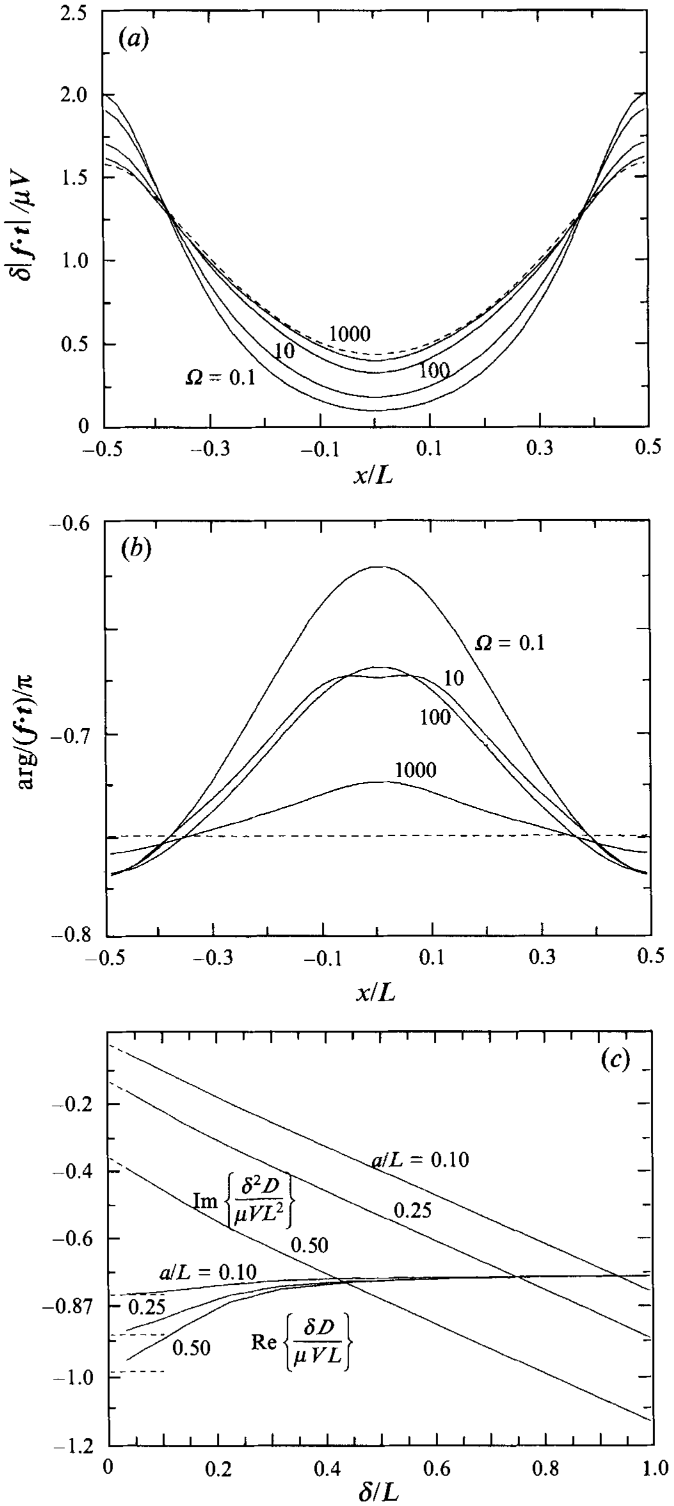

FIGURE 7. For caption see facing page.

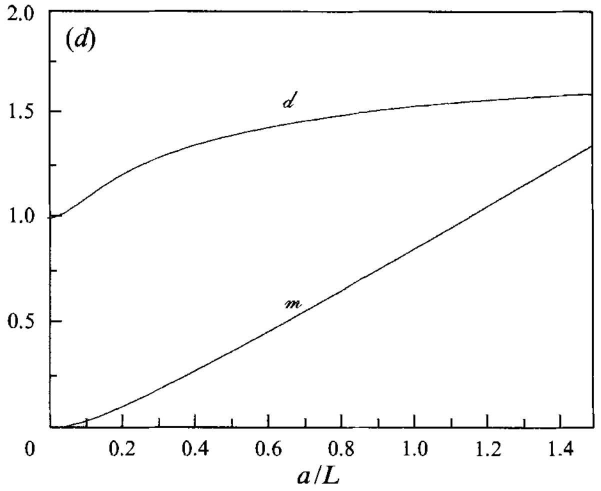

FIGURE 7. The distribution of (*a*) reduced magnitude and (*b*) phase shift of the shear stress on a sinusoidal wall with amplitude $a/L = 0.10$ executing transverse oscillations at several frequencies. The dashed lines represents the asymptotic limit at large frequencies obtained from the potential flow solution. (*c*) The reduced real and imaginary parts of the drag force for several wall amplitudes; the dashed lines are predictions of the asymptotic expansion (3.4). (*d*) Graphs of the virtual mass $\mathscr{m}$ and drag coefficient $\mathscr{d}$ as functions of wall amplitude $a/L$.

where $\boldsymbol{n}$ is the unit normal vector pointing into the fluid (Batchelor 1967, pp. 357, 407; Landau & Lifshitz 1987, p. 87).

Considering a rough wall with sharp corners, we examine whether $\mathscr{m}$ and $\mathscr{d}$ remain finite and the scaling law (3.1) remains effective in view of the increased energy dissipation at the tips. Inspecting the singularity of the potential flow $\boldsymbol{v}$ in the vicinity of a sharp corner, we find that $\mathscr{m}$ is finite suggesting that the leading order scaling in (3.1) is valid. To assess the corresponding behaviour of the drag coefficient $\mathscr{d}$ we consider the boundary integral of $|\boldsymbol{v}|^2$ in the vicinity of a corner and find that it will have a finite value, unless at least one irregularity takes the shape of a thin flat plate of infinitesimal thickness. In that case, the second-order scaling in (3.1) will not be effective and ought to be replaced by an alternative scaling that reflects the divergence of $\mathscr{d}$. In practice, however, the Stokes-layer approximation will cease to be valid at the tip, and the local energy dissipation will have a large but finite value suggesting that (3.1) will be observed.

Let us consider now walls with self-similar irregularities, and examine the behaviour of $\mathscr{m}$ and $\mathscr{d}$ with increasing refinement of the microstructures leading to fractal shapes. Energy considerations suggest that $\mathscr{m}$ should be insensitive to the microstructure of the wall, and thus to the total surface area of the wall, and must be finite even though the wall length might be infinite. The behaviour of the drag coefficient $\mathscr{d}$ is not as clear. The asymptotic analysis of Koch (1987) suggests that the value of $\mathscr{d}$ tends to diverge as the geometry of a particular class of walls with self-similar rectangular crevices is refined. This includes shapes whose limiting value of the wall length is finite. Further evidence for the divergence of $\mathscr{d}$ will be presented in §3.1.2.

It is useful to decompose $\mathscr{d}$ into two contributions that include the skin friction due to the local structure of the Stokes layer and the form drag due to the global structure of the Stokes layer. The skin friction is proportional to the boundary integral of the tangential component of the irrotational flow $\boldsymbol{v}$ discussed above, but this is equal to $VL$ independently of the wall microstructure. Thus, when $\mathscr{d}$ diverges, the form drag will

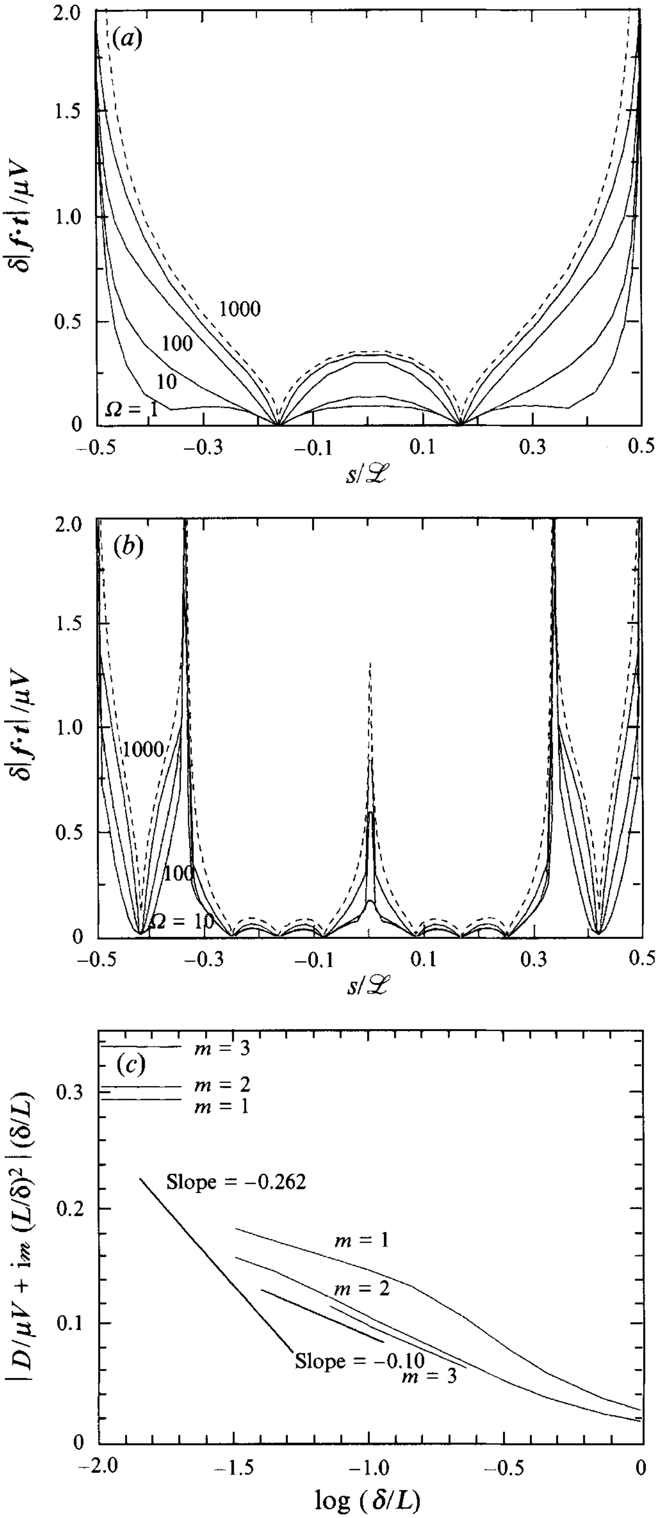

FIGURE 8. For caption see facing page.

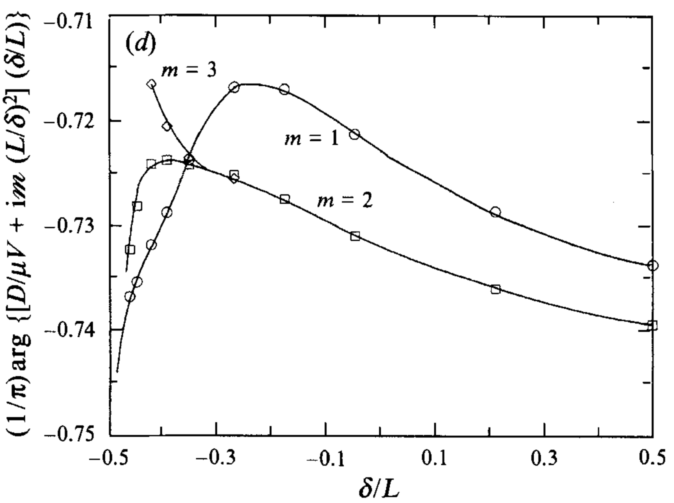

FIGURE 8. The distribution of shear stress on the two von Koch walls illustrated in figure 5(*a*, *b*), for transverse oscillations: (*a*) $m = 1$, (*b*) $m = 2$. The dashed line represents the asymptotic limit at large frequencies. $s$ is the normalized arclength with $s = -0.50$ corresponding to the leftmost point on the contours shown in the insets of figure 5(*a*, *b*). (*c*) The magnitude and (*d*) argument of the dissipative part of the drag force.

make an infinite contribution; the boundary shape will be such that the boundary integral of the tangential component of $\boldsymbol{v}$ is finite but the boundary integral of $|\boldsymbol{v}|^2$ assumes an infinite value.

When it is true that the value of $\mathscr{d}$ diverges for a particular fractal shape, the second-order scaling in (3.1) will not be valid and ought to be replaced by an alternative form that might show an algebraic dependence on $\delta$ in the form

$$|D + \mathrm{i}\mathscr{m}\,\mu V(L/\delta)^2| \approx \mu V\beta(L/\delta)^{1+\gamma}, \tag{3.3}$$

where $\beta$ and $\gamma$ are two constants. In contrast to the case of longitudinal motion, it is not obvious how, if at all, the exponent $\gamma$ is related to the fractal dimension of the surface.

### 3.1. *Numerical results*

We will now present results of numerical computations using the boundary integral method outlined in Appendix A and the conformal mapping method outlined in Appendix B. First, we shall confirm the validity of the expansion (3.1) for walls with sinusoidal shapes, and then we shall examine its applicability to a class of walls with triangular asperities leading to fractal shapes.

#### 3.1.1. *Sinusoidal walls*

In figure 7(*a*) we plot the distribution of the magnitude of the reduced shear stress $\delta \boldsymbol{f}\cdot \boldsymbol{t}/(\mu V)$ for wall amplitude $a/L = 0.10$; $\boldsymbol{t}$ is the tangent vector. At high frequencies, the distribution of $\delta \boldsymbol{f}\cdot \boldsymbol{t}/(\mu V)$ reduces to that of the tangential velocity of the irrotational flow $\boldsymbol{v}$ represented by the dashed line. This behaviour confirms that, in a frame of reference moving with the wall, the Stokes layer is driven by the outer irrotational flow. The numerical results clearly suggest that the shear stress scales with $1/\delta$. In figure 7(*b*) we plot the corresponding distribution of the reduced phase shift $\arg(\boldsymbol{f}\cdot \boldsymbol{t})/\pi$. At high frequencies $\arg(\boldsymbol{f}\cdot \boldsymbol{t})$ tends to the reference value of $-\frac{3}{4}\pi$ required by the flat-plate solution, thereby demonstrating that the Stokes layer penetrates into the sinusoidal corrugations and wraps around the whole of the surface area of the wall. Additional numerical results, not shown in figures, showed that the magnitude of the normal component of the surface force scales with $1/\delta^2$ in agreement with considerations based on the added mass. The behaviour of the flow for larger wall amplitudes is similar to that illustrated in figure 7(*a*, *b*) but has a more complex structure.

Turning to examine the drag force exerted on the wall, we decompose (3.1) into its real and imaginary parts, thus obtaining the asymptotic expressions

$$\mathrm{Re}\left\{\frac{\delta D}{\mu VL}\right\} = -\frac{1}{\surd 2}\mathscr{d}+\ldots, \quad \mathrm{Im}\left\{\frac{\delta^2 D}{\mu VL^2}\right\} = -\mathscr{m}-\frac{1}{\surd 2}\mathscr{d}\frac{\delta}{L}+\ldots. \tag{3.4}$$

In figure 7(*c*) we plot the left-hand sides of (3.4) versus $\delta/L$ for several wall amplitudes $a/L$, and observe that the numerical results are in perfect agreement with the asymptotic predictions represented by the dashed lines. The values of $\mathscr{m}$ and $\mathscr{d}$ necessary for the computation of the asymptotic results were calculated from (3.2) with $\phi$ computed using the boundary integral method discussed in Appendix A. The values of $\mathscr{m}$ and $\mathscr{d}$ for a range of wall amplitudes are presented in figure 7(*d*). We recall that $\mathscr{d}$ is composed of a skin friction that is independent of the wall amplitude and a form drag due to pressure forces, and use figure 7(*d*) to find that as the wall amplitude is increased, the form drag due to normal stresses increases in a monotonic fashion and at an appreciable rate.

### 3.1.2. *Triangular asperities and fractal walls*

In figure 8(*a*, *b*) we plot the distribution of the magnitude of shear stress for the first two von Koch shapes $\alpha = 0.50$, $m = 1, 2$. In both cases, at high frequencies we obtain the potential flow limit represented by the dashed line. The shear stress becomes either zero or infinite at the corners depending on the magnitude of the turning angle. With the exception of the corner behaviour, the general features of the flow are similar to those for sinusoidal walls discussed in §3.1.1. Extensive computations for $m = 3$ at large and small frequencies could not be carried out with sufficient resolution owing to the large size of the resulting system of linear equations as well as excessive computational cost required for computing the Green's function.

Considering next the drag force on the wall, we examine the behaviour of the drag coefficients $\mathscr{m}$ and $\mathscr{d}$ with increasing wall refinement. Using the boundary integral method to obtain the velocity potential $\phi$ we were able to compute the value of $\mathscr{m}$ accurate to the third significant figure for $m = 1, 2$, but not for higher levels. Computing the value of $\mathscr{d}$ using the boundary integral method involves differentiating discrete values of $\phi$ to obtain the boundary velocity, but this yields appreciable numerical error even for the simplest case $m = 1$.

As an alternative, we developed a conformal mapping method that is based on the iterative computation of a modified Swartz–Christoffel function discussed in Appendix B. Values of $\mathscr{m}$ and $\mathscr{d}$ computed using this method are tabulated in table 1 for three families of wall shapes to the accuracy shown. Results for high-order shapes and geometries with sharp asperities, at values of $\alpha$ close to 1, were prohibited by a failure of the numerical method to converge owing to crowding of the vertices in the image plane.

The data in table 1 clearly indicate that, as the order of the wall is increased, $\mathscr{m}$ converges to a finite value thereby implying that the leading-order scaling in (3.1) remains valid. It is interesting to note in particular that for $\alpha = 0.50, 0.80$, the value of $\mathscr{m}$ actually decreases as the wall is refined to the next level. The drag coefficient $\mathscr{d}$, on

| | $\alpha = 0.35$ | | $\alpha = 0.50$ | | $\alpha = 0.08$ | |
|---|---|---|---|---|---|---|
| $m$ | $\mathscr{m}$ | $\mathscr{d}$ | $\mathscr{m}$ | $\mathscr{d}$ | $\mathscr{m}$ | $\mathscr{d}$ |
| 1 | 0.01373 | 1.06196 | 0.15720 | 1.9561 | 0.5055 | 7.941 |
| 2 | 0.02251 | 1.2457 | 0.1527 | 2.005 | 0.475 | 7.135 |
| 3 | 0.02363 | 1.3579 | 0.150 | 2.116 | | 8.11 |
| 3 | 0.02378 | 1.457 | | 2.44 | | |
| 5 | 0.0238 | 1.557 | | | | |

TABLE 1. The added mass coefficient $\mathscr{m}$ and drag coefficients $\mathscr{d}$ for walls with triangular asperities

the other hand, appears to increase by a constant factor that is close to one as the wall is refined to the next level. This behaviour allows for the possibility that in the limit of a fractal geometry $\mathscr{d}$ becomes infinite and the second-order scaling in (3.1) ceases to be valid.

To examine the applicability of the alternative dissipative scaling (3.3), in figure 8(*c*, *d*) we plot the dimensionless magnitude and argument of the dimensionless modified drag force $|D/(\mu V)+\mathrm{i}\mathscr{m}(L/\delta)^2|(\delta/L)$ with respect to $\delta/L$ on a log–log scale and a log–linear scale respectively. At small values of $\delta/L$, the magnitude of the modified drag force tends to the corresponding value of $\mathscr{d}$ represented by a horizontal line in figure 8(*c*) and shown in table 1. The central portions of the curves in figure 8(*c*) may be approximated with straight lines with slopes roughly equal to $\gamma = -0.10$. This value is clearly different from $d = -0.262$ which is the negative of the fractal dimension of the von Koch fractal expressing the gain in wall length with increasing $m$, discussed in §2. It is interesting to note that the slope $\gamma$ is approximately equal to $1-\chi$ where $\chi$ the ratio of two values of $\mathscr{d}$ at two successive values of $m$ deduced from table 1. This observation corroborates the accuracy of the effective boundary surface area theory, and suggests that $\chi$ rather than $d$ should be used in scaling the magnitude of the dissipative drag force.

The argument of the modified drag force, shown in figure 8(*d*), tends to $-\frac{3}{4}\pi$ at both small and large frequencies in agreement with (3.1). As in the case of longitudinal oscillations, the value of $\delta/L$ where the argument is maximum is shifted to smaller values as $m$ is increased.

Insight into the effect of boundary shape on the viscous dissipation and drag force may be obtained by considering the contribution of each boundary segment to the dissipation integral shown in (3.2). In figure 9(*a*, *b*) we plot the value of the dissipation integral over each segment reduced by the length of the segment versus normalized arclength corresponding go the mid-point of each segment on a log–linear scale, for $\alpha = 0.50$ and $m = 3, 4$. The origin of the arclength was set at the leftmost point of the contours shown in the insets. We observe that the contribution to the total dissipation drops by several orders of magnitude within the nested cavities. Comparing figure 9(*a*) to figure 9(*b*) shows that the lowest contribution to the dissipation drops by almost one order of magnitude as $m$ increases to the next level. This drastic decay would appear to suggest that as $m$ tends to infinity $\mathscr{d}$ tends to a finite value, but table 1 suggests otherwise.

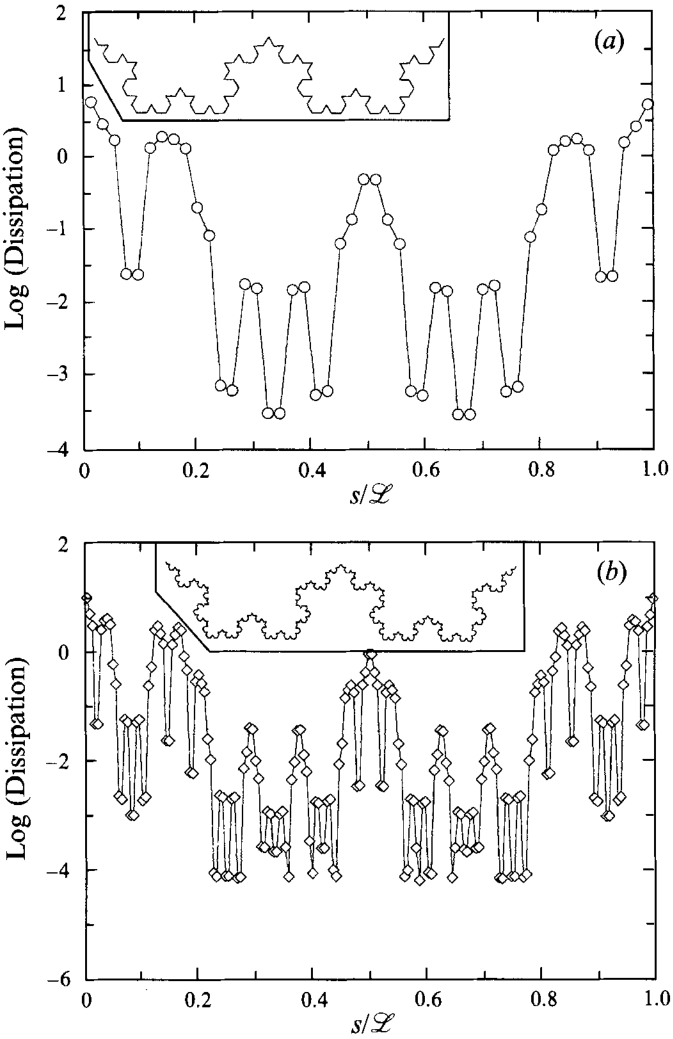

FIGURE 9. The contribution of the boundary segments to the dissipation integral (3.2) reduced with respect to the arclength of the segment, as a function of normalized arclength $s$ of the mid-point of a segment, for $\alpha = 0.50$ and (a) $m = 3$, (b) $m = 4$. $s = 0$ corresponds to the leftmost point on the contours shown in the insets. One period is shown.

## 4. Discussion

Using a two-dimensional flow model we demonstrated the importance of wall roughness on the behaviour of the drag force. Our results for longitudinal motion provide an explicit example in which the magnitude of the drag force and rate of dissipation diverge according to the fractal dimension of the surface. In view of the strong restrictions on the boundary geometry and direction of flow, however, it is not likely that this behaviour is representative of more general motions. Our results for transverse oscillations suggest that the dissipative scaling of the drag force may be altered owing to the presence of an infinite sequence of self-similar irregularities, but not in a way that is related directly to the fractal dimension of the microstructure. This is in agreement with the conclusions of the asymptotic analysis of Koch (1987) for a difference class of boundary shapes.

Generalizing (2.1) and (3.1) to planar walls with three-dimensional irregularities, we write

$$\boldsymbol{D} = \mu[(L/\delta)^2\, \boldsymbol{\mathscr{m}} \cdot \boldsymbol{V} \mathrm{e}^{-\frac{1}{2}\pi \mathrm{i}} + L/\delta\, \boldsymbol{\mathscr{d}} \cdot \boldsymbol{V} \mathrm{e}^{-\frac{3}{4}\pi \mathrm{i}} + \ldots]. \tag{4.1}$$

Here $\boldsymbol{\mathscr{m}}$ is a $3 \times 2$ dimensionless added mass tensor associated with the irregularities, $\boldsymbol{\mathscr{d}}$ is a $3 \times 2$ dimensionless drag coefficient tensor, and $\boldsymbol{V}$ is the amplitude of the wall velocity in the $(x, z)$-plane. Energy arguments suggest that $\boldsymbol{\mathscr{m}}$ must be finite irrespectively of the wall microstructure. Our results in §§2 and 3 indicate that the behaviour of $\boldsymbol{\mathscr{d}}$, and thus the validity of the second-order scaling in (4.1), depend upon the particular geometry of the microstructure and mode of motion. In §2 we found that in the case of two-dimensional fractal walls, the $(x, z)$-component of $\boldsymbol{\mathscr{d}}$ diverges at an algebraic rate that is related to the fractal dimension of the surface. In §3 we found that the $(x, x)$-component of $\boldsymbol{\mathscr{d}}$ may diverge but not in a way that is related directly to the fractal dimension of the surface.

Some information on the behaviour of $\boldsymbol{\mathscr{d}}$ for three-dimensional surfaces is provided by the experimental observations of Warner & Beamish (1987) on the attenuation of ultrasonic waves in porous ceramics filled with liquid helium at high frequencies. Warner & Beamish found that the functional form of attenuation versus frequency deviates from that observed for smooth porous surfaces, and interpreted their results to mean that the pore surface involves a variety of lengthscales comparable to $\delta$, thus deducing a fractal dimension for the microstructure. In the context of (4.1), their results imply that the drag coefficient $\boldsymbol{\mathscr{d}}$ diverges and the second-order dissipative scaling in (4.1) is not valid. This interpretation, however, is subject to criticism (Gist 1989; Warner & Beamish 1989).

The presence of weak inertial forces will cause the onset of a steady streaming motion and development of associated steady shear and normal boundary stresses. Because of the symmetry of the geometries considered, the steady drag force exerted over one period of the wall will be equal to zero, and the dominant contribution to the force will still be given by the unsteady drag due to the linear motion. Strong inertial forces will complicate the physics of the flow in several important ways. First, the alternating ejection of vortex sheets of opposite sign from regions of large curvature and sharp corners will allow vortex motions and flow instabilities. Secondly, it is likely that the flow will not remain periodic in time.

Concluding, we place the problem of oscillatory flow over irregular surfaces within the more general framework of transport processes across rough and fractal boundaries. Fractal geometries have been shown to describe a wide variety of natural surfaces (Avnir, Farin & Pfeiffer 1984, Katz & Thompson 1985), and their study is relevant to a number of transport processes occurring in natural and engineering applications. The functional relationship between drag and frequency may be regarded as a diagnostic that allows one to characterize the boundary microstructure and possibly resolve its fractal nature. Analogous functional forms relating macroscopic flow variables to frequency have been proposed as a tool for characterizing the structure of porous media (Charlaix, Kushnick & Stokes 1988; Warner & Beamish 1987). In these applications, the functional form of the scaling law undergoes a transition from a viscous-dominated regime to an inertia-dominated regime, at that point where the nominal thickness of the Stokes layer becomes comparable to the size of the grains composing the porous medium. The present work suggests that measured macroscopic scaling laws do not necessarily yield accurate information on the geometry of the microstructure.

Thanks are due to Professors P. Dimotakis, D. Koch, A. Acrivos, and Dr E. J.

Hinch for helpful discussions and comments on the manuscript. This work is supported by the National Science Foundation, Grant CTS-9216176, the Exxon Education Foundation, and the Eastman Kodak Company.

## Appendix A

In this Appendix we outline a boundary integral method for computing the flow due to the longitudinal or transverse oscillations of the wall illustrated in figure 1. To simplify the notation, we reduce all variables using as characteristic length, velocity, and stress scales the period of the wall $L$, the amplitude of the velocity $V$, and $\mu V/L$.

### A.1. *Longitudinal oscillations*

We express the $z$-component of the velocity in the form $w = W(x,y)\,\mathrm{e}^{\mathrm{i}\omega t}$ and substitute into the Navier–Stokes equation to obtain the Helmholtz equation $\lambda^2 W = \nabla^2 W$ where $\lambda^2 = \mathrm{i}\omega L^2/\nu$. We define $\lambda$ to be the primary square root of $\lambda^2$ with positive real part, setting $\lambda = (L/\delta)\,\mathrm{e}^{\frac{1}{4}\pi\mathrm{i}}$. Using the boundary integral formulation for the Helmholtz equation, which is identical to Green's third identity, and requiring the boundary condition $W = 1$ over the wall, we obtain a Fredholm integral equation of the first kind for the wall shear stress $q = \boldsymbol{\nabla} W \cdot \boldsymbol{n}$,

$$\int_C G(\boldsymbol{x},\boldsymbol{x}_0)\,q(\boldsymbol{x})\,\mathrm{d}l(\boldsymbol{x}) = -\tfrac{1}{2} + \int_C^{PV} \boldsymbol{\nabla} G(\boldsymbol{x},\boldsymbol{x}_0)\cdot\boldsymbol{n}(\boldsymbol{x})\,\mathrm{d}l(\boldsymbol{x}), \tag{A 1}$$

where $C$ is the trace of the wall in the $(x,y)$-plane as indicated in figure 1, the point $\boldsymbol{x}_0$ is located on $C$, $PV$ denotes the principal value of the double-layer integral, and $\boldsymbol{n}$ is the normal vector pointing into the fluid. $G$ is the periodic Green's function of the Helmholtz equation, defined as a solution to the equation

$$\nabla^2 G(\boldsymbol{x},\boldsymbol{x}_0) - \lambda^2 G(\boldsymbol{x},\boldsymbol{x}_0) + \sum_{n=-\infty}^{\infty} d(\boldsymbol{x}-\boldsymbol{x}_n) = 0, \tag{A 2}$$

where $\boldsymbol{x}_n = (x_0 + nL, y_0)$ and $d$ is the two-dimensional delta function. We find

$$G(\boldsymbol{x},\boldsymbol{x}_0) = \frac{1}{2\pi}\sum_{n=-\infty}^{\infty}[\mathrm{ker}_0(R_n) + \mathrm{i}\,\mathrm{kei}_0(R_n)] \tag{A 3}$$

where $R_n = Lr_n/\delta$, $r_n = |\boldsymbol{x}-\boldsymbol{x}_n|$, and ker, kei are the real and imaginary Kelvin functions of zeroth order (Abramowitz & Stegun 1965). Since these functions decay at an exponential rate for large values of their arguments, the sum in (A 3) may be conveniently truncated to a finite value of $n$ that depends on the magnitude of $\delta/L$.

### A.2. *Transverse oscillations*

We write $\boldsymbol{u} = \boldsymbol{U}(x,y)\,\mathrm{e}^{\mathrm{i}\omega t}$, $P = p(x,y)\,\mathrm{e}^{\mathrm{i}\omega t}$, and substitute these expressions into the Navier–Stokes equations to obtain

$$\lambda^2 \boldsymbol{U} = -\boldsymbol{\nabla} p + \nabla^2 \boldsymbol{U}. \tag{A 4}$$

The problem is reduced to solving (A 4) along with the continuity equation $\boldsymbol{\nabla}\cdot\boldsymbol{U} = 0$, subject to the boundary condition $\boldsymbol{U} = (1,0,0)$ along the wall. Using the boundary integral formulation (Pozrikidis 1992), we obtain the following Fredholm integral equation of the first kind for the boundary distribution of the surface force $\boldsymbol{f} = \boldsymbol{\sigma}\cdot\boldsymbol{n}$:

$$\int_C \mathcal{S}_{ij}(\boldsymbol{x},\boldsymbol{x}_0)\,f_i(\boldsymbol{x})\,\mathrm{d}l(\boldsymbol{x}) = -2\pi\,\delta_{1j} + \int_C^{PV} \mathcal{T}_{1jk}(\boldsymbol{x},\boldsymbol{x}_0)\,n_k(\boldsymbol{x})\,\mathrm{d}l(\boldsymbol{x}), \tag{A 5}$$

where $\boldsymbol{\sigma}$ is the stress tensor, and the point $\boldsymbol{x}_0$ is located on the wall contour $C$. $\mathcal{S}$ is the periodic Green's function corresponding to (A 4), defined as a solution to the equation

$$\nabla^2 \mathcal{S}_{ij}(\boldsymbol{x},\boldsymbol{x}_0) - \lambda^2 \mathcal{S}_{ij}(\boldsymbol{x},\boldsymbol{x}_0) - \frac{\partial p_j}{\partial x_i}(\boldsymbol{x}-\boldsymbol{x}_0) + 4\pi\,\delta_{ij} \sum_{n=-\infty}^{\infty} d(\boldsymbol{x}-\boldsymbol{x}_n) = 0; \tag{A 6}$$

$p$ and $\mathcal{T}$ are the corresponding Green's functions for the pressure and stress tensor related by $\mathcal{T}_{ijk} = -\delta_{ik}\,p_j + \partial\mathcal{S}_{ij}/\partial x_k + \partial\mathcal{S}_{kj}/\partial x_i$. Following a standard procedure for computing the Green's functions of the equations of linearized fluid flow (Pozrikidis 1992, Chap. 3), we find

$$\mathcal{S}(\boldsymbol{x},\boldsymbol{x}_0) = \boldsymbol{I} \sum_{n=-\infty}^{\infty} A(R_n) + \sum_{n=-\infty}^{\infty} \frac{\hat{\boldsymbol{x}}_n \hat{\boldsymbol{x}}_n}{|\hat{\boldsymbol{x}}_n^2|} B(R_n) + \mathrm{i}\frac{\delta^2}{L^2} \boldsymbol{\nabla\nabla} C(\hat{\boldsymbol{x}}_0), \tag{A 7}$$

$$p(\boldsymbol{x},\boldsymbol{x}_0) = -\boldsymbol{\nabla} C(\hat{\boldsymbol{x}}_0), \tag{A 8}$$

where $\boldsymbol{I}$ is the identity matrix, $\hat{\boldsymbol{x}}_n = \boldsymbol{x}-\boldsymbol{x}_n$, i is the imaginary unit, and the functions $A, B, C$ are defined as

$$A(x) = 2[\mathrm{ker}_0(x) - \mathrm{kei}_0'(x)/x] + 2\mathrm{i}[\mathrm{kei}_0(x) - \mathrm{ker}_0'(x)/x], \tag{A 9}$$

$$B(x) = 2[-\mathrm{ker}_0(x) + 2\,\mathrm{kei}_0'(x)/x] - 2\mathrm{i}[\mathrm{kei}_0(x) + 2\,\mathrm{ker}_0'(x)/x], \tag{A 10}$$

$$C(x) = \log[\cosh(2\pi y) - \cos(2\pi x)]. \tag{A 11}$$

The Kelvin's functions and their derivatives may be approximated with polynomial and exponential expansions (Abramowitz & Stegun 1965, p. 384). Since successive terms in the sums of (A 7) decay at an exponential rate, the sum may be truncated at a finite value of $n$ according to the value of $\delta/L$.

At large frequencies, the flow is composed of an outer irrotational core and a Stokes boundary layer that lines the wall. To compute the outer flow we solve the following Fredholm integral equation of the first kind for the distribution of the velocity potential $\phi$ along one period of the wall:

$$\int_C^{PV} \boldsymbol{\nabla}\mathcal{G}(\boldsymbol{x}-\boldsymbol{x}_0)\cdot\boldsymbol{n}(\boldsymbol{x})\,\phi(\boldsymbol{x})\,\mathrm{d}l(\boldsymbol{x}) = \tfrac{1}{2} + \int_C \mathcal{G}(\boldsymbol{x}-\boldsymbol{x}_0)\,n_1(\boldsymbol{x})\,\mathrm{d}l(\boldsymbol{x}). \tag{A 12}$$

$\mathcal{G}$ is the periodic fundamental solution of the two-dimensional Laplace equation. This is equal to $(1/\pi)\,C$ where the function $C$ is given in (A 11).

### A.3. *Numerical method*

The numerical procedure for solving the integral equations proceeds by discretizing the trace of the wall over one period $C$ into a set of straight boundary segments, assuming that the unknown function is constant over each segment, and then applying the integral equations at the middle point of each segment to obtain a system of linear equations for the constant values of the unknown function. The singular single-layer integrals are computed by subtracting the logarithmic singularities of the kernels and then performing analytical integrations. The desingularized single-layer integrals and principal values of the double-layer integrals are computed using the six-point Gaussian quadrature. Since the collocation points are located at the middle of each segment, no special treatment of the principal values of the double-layer integrals is necessary, and ignoring the singularities yields accurate results.

The numerical procedure works well even when the boundary contains sharp corners where the solution becomes infinite. In these cases, the accuracy of the computations is significantly improved by concentrating the boundary elements around the corners. An alternative procedure in which the singular behaviour of the solution is taken into

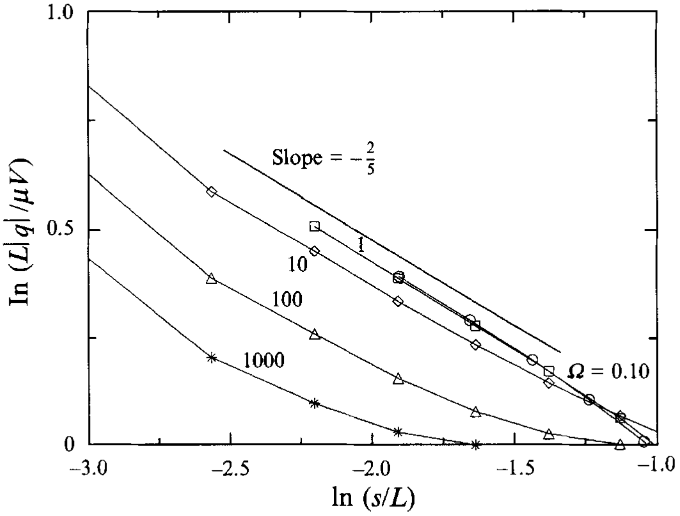

FIGURE 10. The distribution of shear stress near a boundary corner for longitudinal oscillations. A local similarity solution predicts a slope of $-\frac{2}{5}$ at all frequencies.

| (*a*) | $\eta$ | $K = 4$ | $K = 8$ | $K = 16$ |
|---|---|---|---|---|
| | 1.0 | 1.3462 | 1.3499 | — |
| | 1.50 | 1.3478 | 1.3515 | — |
| | 1.75 | 1.3483 | 1.3519 | 1.3527 |
| | 2.00 | 1.3487 | 1.3521 | — |

| (*b*) | $\eta$ | $K = 4$ | $K = 8$ | $K = 16$ | $K = 32$ |
|---|---|---|---|---|---|
| | 1.0 | 27.331 | 27.594 | 27.688 | 27.737 |
| | 1.50 | 27.604 | 27.834 | 27.872 | 27.880 |
| | 1.75 | 27.680 | 27.682 | 27.880 | — |

TABLE 2. Magnitude of the drag force for longitudinal oscillations as a function of numerical parameters for (*a*) longitudinal oscillations and (*b*) transverse oscillations

consideration in the numerical implementation did not offer significant improvements. In figure 10 we plot the distribution of shear stress versus arclength measured from a sharp corner of a von Koch line on a log–log scale, at different frequencies for longitudinal oscillation. The slopes of the lines at all frequencies are close to the value $-\frac{2}{5}$ which is predicted by a local similarity solution.

In table 2 we show the magnitude of the computed drag force on the $m = 1$ von Koch line for longitudinal and transverse motion as a function of the number of segments over each side $K$ and the amplification $\eta$ of the length of the segments from the corner to the centre of a side; $\eta = 1$ corresponds to an even distribution. We observe a rapid convergence which is in agreement with theoretical predictions for boundary element solutions with piecewise-constant discretizations near singular points (Chandler & Graham 1988). These results indicate that the numerical method is capable of accurately computing global variables with a moderate number of elements.

In the majority of our computations we used values of $\eta$ in the range 1.50 to 1.75. For longitudinal oscillations with $m = 1, 2, 3$ we used $K = 32, 16, 8$, and for lateral oscillations $K = 16, 8, 6$. In many cases, Richardson extrapolation with quadratic accuracy was used to improve the accuracy of the computed drag force.

## Appendix B

In this Appendix we outline a conformal mapping method suitable for computing streaming potential flow over a periodic polygonal wall as illustrated in figure 11, as well as the associated virtual mass and drag coefficients defined in (3.2). The domain of flow above the polygonal wall in the physical plane $z = x+\mathrm{i}y$ is mapped onto the upper-half plane $\zeta = \zeta+\mathrm{i}\eta$ using the modified Swartz–Christoffel mapping function $\mathrm{d}z/\mathrm{d}\zeta = G(\zeta)$ where

$$G(\zeta) = C\prod_{i=1}^{N}\left(\sin\frac{\pi(\zeta-a_i)}{a_{N+1}}\right)\alpha_i. \tag{B 1}$$

$C$ is a complex constant, $a_i$, $i = 1,\ldots,N+1$ are the images of the vertices $z_i$ within one period of the physical plane, and $\pi\alpha_i$ are the corresponding turning angles. These are positive for sharp corners and negative for blunt corners, as illustrated in figure 11.

To render the mapping function unique, we stipulate the magnitude of $C$ is equal to one, and set the first image point at the origin, $a_1 = 0$. The remaining $N$ unknowns include the argument of $C$ and the location of the $N$ vertices $a_i$, $i = 2,\ldots,N+1$. Following Davis (1979) and Brady & Pozrikidis (1993), we compute the solution by the following iterative procedure. We set $C = 1$, guess values for the unknown $a_i$, and calculate the location of successive vertices by computing

$$z_{i+1}^{C} = z_i^{C} + \int_{a_i}^{a_{i+1}} G(\xi)\,\mathrm{d}\xi, \tag{B 2}$$

with $z_1^C = z_1$, the superscript $C$ signifying 'computed'. We then update the position of $a_i$ by setting

$$|a_{i+1}^{New}-a_i^{New}| = |a_{i+1}-a_i|\frac{|z_{i+1}-z_i|}{|z_{i+1}^{C}-z_i^{C}|}. \tag{B 3}$$

The procedure is repeated until the values of $a_i$ do not change to the seventh decimal place. At the end of the iterations, the value of $a_{N+1}$ is equal to $L$. Since the complex function $G(\xi)$ is evaluated as

$$G(\xi) = C\exp\left\{\sum_{i=1}^{N}\left[\alpha_i\log\left|\sin\frac{\pi(\xi-a_i)}{a_{N+1}}\right| + \mathrm{i}\alpha_i\arg\left(\sin\frac{\pi(\xi-a_i)}{a_{N+1}}\right)\right]\right\}, \tag{B 4}$$

where the argument in the last term in (B 4) is either 0 or $\pi$, the last segment $z_{N+1}^C - z_N^C$ is horizontal and the computed polygon is rotated by a certain angle with respect to the original polygon in the $z$-plane. To make the two polygons coincide, at the end of the iterations we perform a rotation by adjusting the argument of the complex constant $C$ to a proper value.

We find that the number of iterations is a strong function of the number of vertices and the shape of the wall, typically ranging between 3 for the simplest and 50 for the most difficult computations. Crowding of the vertices on the $\xi$-axis decelerates the rate of convergence and allows oscillatory behaviour. Using dynamic continuation to obtain a good initial value reduces the number of iterations but does not eliminate numerical oscillations and slow convergence.

The complex potential for uniform flow with velocity $V$ along the $x$-axis is given by $w = V\zeta$. Using (3.2) we find that added mass coefficient $\mathscr{m}$ and drag coefficient $\mathscr{d}$ may be computed from the mapping function $G$ by straightforward integration as

$$\mathscr{m} = \frac{1}{L^2}\int_{Wall} x\,\mathrm{d}y - \frac{1}{L^2}\int_{a_1}^{a_{N+1}} \xi\,\mathrm{Im}\,[G(\xi)]\,\mathrm{d}\xi, \quad \mathscr{d} = \frac{1}{L}\int_{a_1}^{a_{N+1}} \frac{1}{|G(\xi)|}\mathrm{d}\xi. \tag{B 5}$$

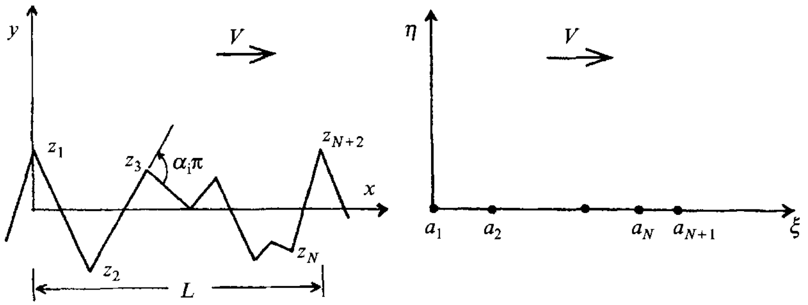

FIGURE 11. Conformal mapping of a periodic polygonal line to a straight line.

The singular integrals in (B 2) and (B 5) were computed by subtracting and integrating analytically the kernels of the singularities, and then applying the 6, 12, or 20 Gauss–Legendre quadrature to integrate the remaining regular component.

## REFERENCES

ABRAMOWITZ, M. & STEGUN, I. A. 1965 *Handbook of Mathematical Functions*. Dover.

AVNIR, D., FARIN, D. & PFEIFER, P. 1984 Molecular fractal surfaces. *Nature* **308**, 261–263.

BATCHELOR, G. K. 1967 *An Introduction to Fluid Dynamics*. Cambridge University Press.

BRADY, M. A. & POZRIKIDIS, C. 1993 Diffusive transport across irregular and fractal walls. *Proc. R. Soc. Lond.* A **442**, 571–583.

CHANDLER, G. A. & GRAHAM, I. G. 1988 Product integration-collocation methods for noncompact integral operator equations. *Math. Comput.* **50**, 125–138.

CHARLAIX, E., KUSHNICK, A. P. & STOKES, J. P. 1988 Experimental study of dynamic permeability in porous media. *Phys. Rev. Lett.* **61**, 1595–1598.

DAVIS, R. T. 1979 Numerical methods for coordinate generation based on Schwartz–Christoffel transformations. *Proc. 4th Am. Inst. Aero. Astro. CFD Conf., Williamsburgh, VA.*

FEDER, J. 1988 *Fractals*. Plenum.

GIST, G. A. 1989 Ultrasonic attenuation and fractal surfaces in porous media. *Phys. Rev.* B **39**, 7295–7297.

JOHNSON, D. L., KOPLIK, J. & DASHEN, R. 1987 Theory of dynamic permeability and tortuosity in fluid-saturated porous media. *J. Fluid Mech.* **176**, 379–402.

KANEKO, A. & HONJI, H. 1979 Double structure of steady streaming in the oscillatory viscous flow over a wavy wall. *J. Fluid Mech.* **93**, 727–736.

KATZ, A. J. & THOMPSON, A. H. 1985 Fractal sandstone pores: implications for conductivity and pore formation. *Phys. Rev. Lett.* **54**, 1325–1328.

KOCH, D. L. 1987 Attenuation of a compressional sound wave in the presence of a fractal boundary. *Phys. Fluids* **30**, 2922–2927.

LANDAU, L. D. & LIFSHITZ, E. M. 1987 *Fluid Mechanics*, 2nd edn. Pergamon.

LYNE, W. H. 1971 Unsteady viscous flow over a wavy wall. *J. Fluid Mech.* **50**, 33–48.

POZRIKIDIS, C. 1992 *Boundary Integral and Singularity Methods for Linearized Viscous Flow*. Cambridge University Press.

RALPH, M. E. 1986 Oscillatory flows in wavy-walled tubes. *J. Fluid Mech.* **168**, 515–540.

SOBEY, I. J. 1980 On flow through furrowed channels. Part 1. Calculated flow patterns. *J. Fluid Mech.* **96**, 1–26.

WARNER, K. L. & BEAMISH, J. R. 1987 Ultrasonic attenuation and pore microstructure in a liquid-$^4$He-filled ceramic. *Phys. Rev.* B **36**, 5698–5701.

WARNER, K. L. & BEAMISH, J. R. 1989 Reply to comment 'Ultrasonic attenuation and fractal surfaces in porous media'. *Phys. Rev.* B **39**, 7298–7299.